Desalination and Water Treatment
www.deswater.com

doi: 10.5004/dwt.2019.23562

143 (2019) 274–281
March

Tailoring the properties of nanocrystalline multiferroic $BiFeO_3$ by simultaneous substitution of Bi^{3+} and Fe^{3+} metal cations for enhanced visible-light-driven photocatalysis

Sajjad Ahmad[a], Muhammad Suleman[b], Sara Musaddiq[c], Najeeb Fuad Al-Khalli[d], Philips Olaleye Agboola[e], Aziz-ur-Rehman[a,*], Imran Shakir[f], Muhammad Azhar Khan[g], Muhammad Farooq Warsi[a,*]

[a]*Department of Chemistry, Islamia University of Bahawalpur, Bahawalpur 63100, Pakistan, emails: azizypk@yahoo.com (Aziz-ur-Rehman); farooq.warsi@iub.edu.pk (M.F. Warsi)*
[b]*Department of Agricultural Chemistry, The University of Agriculture, Peshawar, Pakistan*
[c]*Department of Chemistry, The Women University, Multan, Pakistan*
[d]*Department of Electrical Engineering, King Saud University, Riyadh 11421, Kingdom of Saudi Arabia*
[e]*College of Engineering Al-Muzahmia Branch, King Saud University, PO-BOX 800, Riyadh 11421, Kingdom of Saudi Arabia*
[f]*Sustainable Energy Technologies Center, College of Engineering, King Saud University, Riyadh 11421, Kingdom of Saudi Arabia*
[g]*Department of Physics, The Islamia University of Bahawalpur, Bahawalpur 63100, Pakistan*

Received 20 April 2018; Accepted 30 November 2018

ABSTRACT

Multiferroic ceramics ($BiFeO_3$) co doped with Yb and Ni cations ($Bi_{1-x}Yb_xNi_yFe_{1-y}O_3$) were synthesized via micro-emulsion route. The dopant (Yb and Ni) contents were fixed $x = 0.0 < x > 0.125$ and $y = 0.0 < x > 0.25$ for six different compositions. The fabricated ceramics were examined with various techniques to index certain features such as crystal habitat, electrical, dielectric, magnetic, and photocatalytic properties. Fourier-transform infrared spectroscopy, X-ray diffraction (XRD), ultraviolet/visible spectroscopy, impedance analyzer constant, current–voltage (I–V) behavior, and vibrating sample magnetometer (VSM). XRD crews revealed a highly crystalline rhombohedral (R3c) structure growth on inclusion of ytterbium and nickel cations in $BiFeO_3$ ceramics. However, on substituent concentrations, $x = 0.125$, $y = 0.25$ moles, the diffraction pattern (111) against $2\theta = 27°$ showed a phase transformation from rhombohedral to orthorhombic phase. Nanocrystalline morsels were harvested with sizes ~21–23 nm. The fabricated ceramics exhibited the resistivity $1.4 \times 10^9\ \Omega\ cm^{-1}$. The VSM analysis of fabricated ceramics revealed a notable enhancement of magnetization up to 1.51 emu/g for $x = 0.1$, $y = 0.2$ moles. The ceramic composition $Bi_{0.90}Yb_{0.10}Ni_{0.2}Fe_{0.80}O_3$ exhibited the minimum optical band gap 1.25 eV, and these particles showed the photocatalytic activity of >64%. The fabricated ceramic inherited magnetic merits and could be easily removed by applying conventional magnetic bar.

Keywords: Multiferroics; Visible light; Photocatalysis; Ytterbium and nickel co-doped BiFeO3; Congo red; Optical band gap

1. Introduction

Multiferroic materials were considered trivial in past century due to worthless practical applications. Weak electromagnetic coupling and low operational temperatures hampered to customize the multiferroic materials in practices. However, since last decade, a great attraction is being paid to these materials [1]. It has been found that researchers fabricated such multiferroic materials which possessed

* Corresponding authors.

magnetic Ferroelectrics at moderate magnetic field and room temperature. Physiochemical characteristics of these materials depend upon the composition, technique of synthesis, and crystallite size. Therefore, nanoscience is also playing its role in this modern research field of multiferroics [2]. The nanosize magnetic materials exhibited significantly better properties than their bulk counter parts. Multiferroic materials have potential applications in efficient electromagnetic devices, recording media, and sensors which replaced the old technologies [3]. The multiferroic materials were classified into two major classes depending upon their mode of action. The naturally occurring old multiferroic materials were placed as, "Type-I" such as $BiFeO_3$, $BiMnO_4$, $YMnO_4$, etc. Type-II materials are new fabricated multiferroic materials which have improved outputs [4].The worth of multiferroic material could be awarded by analyzing the remnant polarization, remnant magnetization, and an extent of their mutual coupling in a single phase of material.

$BiFeO_3$ (BFO) is unanimously accepted as a standard for multiferroic research due to unique merits of ferromagnetism and polarization above room temperature. The extended features include G-type antiferromagnetic behavior as purposed by Neel at T_N = 350 < 380°C and para-electric phase transitions at Curie temperature (T_C = 850°C). However, the practical applications of BFO are insignificant due to leakage of current and weak coupling of multiferroic orders. BFO possess rhombohedral distorted perovskite structure. ABO_3 having two distorted sub lattice blocks which are joined along their body diagonals by adopting the pseudo cubic structure (111) [5]. Stereo chemical strain of Bi^{3+} lone pair initiates in house dipole moments and consequently displaces body-centered Fe^{3+} cation relative to FeO_6 octahedral lattice cage. Polarization in BFO has been attributed due to Bi and oxygen bond polarity [4]. Occurrence of oxygen vacancies, heterogeneous iron valencies (Fe^{2+}/Fe^{3+}) and impurities such as $Bi_2Fe_4O_9/Bi_{25}Fe4O_{40}$ are main complications which hindered the use of BFO for commercial applications [6–8].

Various attempts had been made by the researchers to combat these complications. One of the most often reported method was to modify the already existing multiferroic materials through substitution of suitable elements. Various metal ions were substituted in BFO such as alkaline earth (Ba, Ca), rare earth (Gd, Nd, La, Pr, Sm), and transition metal cations (Mn, Co, Ni) [9–14]. Substitution of alkaline earth metals cations improved the ferroelectricity of BFO, however the magnetic properties were suppressed and diamagnetic behavior was appeared [15,16].

The researchers remunerated unusual consideration for rare earth cations substitution and discovered encouraging consequence both for ferroelectricity and ferromagnetic properties. In this context, Pradhan and Roul [17] probed the properties of the Gd^{3+} substitution ($Bi_{1-x}Gd_xFeO_3$) and recognized that the photocatalytic capability of the ceramic was boosted. It was also described that dielectric constant as well as the dielectric loss exhibited a significant dispersions at lower frequencies [17]. Chen et al. [18] incorporated La-doped BFO via hydrothermal method, and a normal rhombohedral structure was reported which transformed into orthorhombic at doping concentration (x = 0.20). The dielectric constant deviations were observed near the Neel temperature (T_N). An appropriate coupling between ferroelectricity and ferromagnetic parameters with enhanced insulating property was also reported [18]. The stimuli of Sm doping were described by Zhang et al. They synthesized the ($Bi_{1-x}Sm_xFeO_3$) via solid state reaction. It was observed that the doping of Sm^{3+} in $BiFO_3$ enhanced the multiferroic properties by supporting the formation of perovskite structure and eliminating the secondary phases such as $Bi_{25}FeO_{40}$. Absence of Fe^{2+} ions was also recorded in Sm-doped specimens, which eventually reduced the current leakage [19]. Zhao and Yun [20] synthesized a BFO that was doped with Ho^{3+} and Mn^{4+} metal cations. A significant improvement in magnetic density was observed, and it was established that simultaneous doping of Ho^{3+} cations improved ferromagnetism due to the crystallite distortion which restructured the antiparallel spin arrangements [20]. Similarly, BFO co doped with holmium and nickel metal cations ($Bi_{1-x}Ho_xNi_{1-y}Fe_yO_3$) were manufactured via sol–gel method. The characterization features showed the polycrystalline ceramic with rhombohedral perovskite structure. They found that these ingredients exhibited the maximum magnetic saturation 0.228 emu/g and coercive field 280 Oe [21]. Cui et al. [22] reported an approach to inhibit the toxic intermediate substances during photocatalysis process. For this purpose, they prepared amorphous carbon nitride co-functionalized with O/Ba [22]. Dong et al. [23] reported the theoretical studies on activation of reactants and intermediates. Their main focus was to use the powder photocatalyst for selective conversion of compounds of interest [23]. Xiong et al. [24] used ternary composite approach for enhanced photocatalytic applications. They prepared the ternary composite of Ag, AgCl, and $BiOIO_3$ by cheap route [24]. Li et al. [25] reported the modified C_3N_4 nanosheets for visible-light-driven photocatalysis applications. They used thermal condensation approach for synthesis of graphitic carbon, which has graphene-like structure [25].

$Bi_{1-x}Ln_{0.05}Co_{0.05}FeO_3$ (Ln = La and Pr) co-doped BFO powder materials were reported by Mao et al. [26]. They reported that co doping of La and Co enhanced the multiferroic magnetic parameters. The saturation magnetization was found 0.535 emu/g. Further they found the significant distortion in Fe–O bond [26]. This distortion was supported by Raman spectroscopic data. However, the co doping of lanthanum and manganese metal cations (La^{3+}, Mn^{4+}) in BFO showed a high conductivity [27]. Co doping of Eu and Co in BFO significantly enhanced saturated magnetization by improving the canting angle [28]. Recently, Ni- and Co-doped BFO have been synthesized with enhanced magnetic properties [29]. The materials with optical band gap <3eV are considered as a sunlight energy harvesters. The materials which display body-centered crystal structures are associated with ferroelectricity and usually show electronic transitions in UV/visible region [30–32]. BFO nanoparticles showed a strong absorption band (2.55 eV) in the range of visible light and hold a potential of photocatalytic activities. The photocatalytic potential of BFO was evaluated through photocatalytic degradation of textile dyes such as Congo red, Rhodamine–B, etc. [33].

2. Experimental setup

$Bi_{1-x}Yb_xNi_y$ $Fe_{1-y}O_3$ nanoparticles synthesis was carried out using following chemicals; $Bi(NO_3)_3.5H_2O$

(99%, Sigma-Aldrich, USA), $Fe(NO_3)_3.9H_2O$ (98% Sigma-Aldrich, USA), Yb $(NO_3)_3.5H_2O$ (99%, Sigma-Aldrich, USA), $(CH_3COO)_2Ni$, (98%, BDH), Cetyltrimethylammonium bromide (98%, Amresco, Canada), aqueous NH_3 (35%, BDH), and concentrated nitric acid (HNO_3). All these chemicals were used without any further purification. Stoichiometric amounts of all the precursors were dissolved in a required volume of deionized water in separate beakers. However the digestion of $Bi(NO_3)_3.5H_2O$ was carried out by concentrated HNO_3. For six different compositions of $Bi_{1-x}Yb_xNi_y\ Fe_{1-y}O_3$ nanoparticles, required quantity of metal salt solutions were mixed in six separate beakers. The mixtures were stirred and heated till 60°C. The heating was stopped and at room temperature, freshly prepared Cetyltrimethylammonium bromide (CTAB) (0.2 M, 100 mL) solution was added to reaction mixtures separately. Freshly prepared aqueous ammonia solution was added to maintain pH of all reaction mixtures to ~10 to 11. Reaction mixtures were continuous stirred for 5 h and then placed on bench static overnight. Finally brown precipitates were decanted from a viscous layer of CTAB. The reaction precipitates were dried and grinded using agate pestle-mortar. The series of six homogenized samples was sintered at 900°C for 7 h in muffle furnace Vulcan A-550. Then sintered samples were cooled slowly, grinded, and homogenized. The schematic representation of synthetic route is shown in Fig. 1.

3. Characterization of co-doped BFO ceramics

The prepared ceramics were investigated through different techniques to reach the significant data, that is, Fourier-transform infrared (FTIR) spectroscopy, X-ray diffraction (XRD), UV/visible spectroscopy, dielectric constant, current–voltage measurements, and vibrating sample magnetometery (VSM). The optical band gaps of fabricated ceramics were calculated through Tauc plot, and the photocatalytic potential of ceramic was studied through photocatalytic degradation of a textile dye (Congo red).

3.1. XRD analysis

Philips Xpert PRO 3040/60 diffractometer was used to record XRD patterns using radiation source of Cu(K_α). The noted spectra were interpreted by comparing the diffraction patterns of BFO with standard cards available (ICSD:01-086-1518). XRD spectra disclosed a rhombohedral (R3c) crystalline structure on substitution of ytterbium and nickel cations in BFO ceramics. The peak for unsubstituted BFO showed impurities at diffraction angle 35.4°, however with increase in dopants concentrations, a significant improvement was observed. The characteristic BFO peaks were observed against the angle (2θ) = 31.56° and 32.74° with d_{hkl} coordinates [204] and [110], respectively. A maximum pure phase diffraction pattern was observed for doping concentration for x = 0.10 and y = 0.20 moles. The presence of diffraction peak (006) at 2θ = 38.85° proposed the normal rhombohedral (R3c) structure phase on inclusion of Yb and Ni cations (Fig. 2). However for the dopant concentrations (x = 0.125, y = 0.25 moles) the diffraction pattern (111) against 2θ =27° showed a phase transformation from rhombohedral to orthorhombic phase. The spectra of BYNFO series samples showed a wide-ranging agreement with stated reference data card ICDS 01-086-1518. The various parameters of crystallites were calculated by applying the proper equations as summarized in Table 1. The lattice parameters of each composition were calculated from a, b, and c coordinates as derived from diffraction plane coordinates hkl.

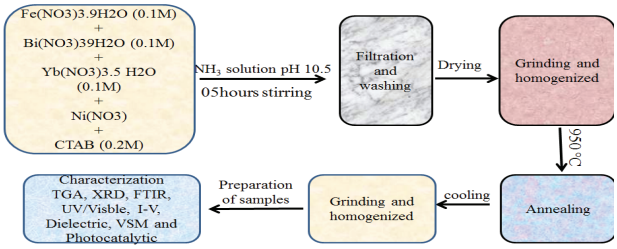

Fig. 1. Schematic diagram for fabrication steps of BYNFO, series.

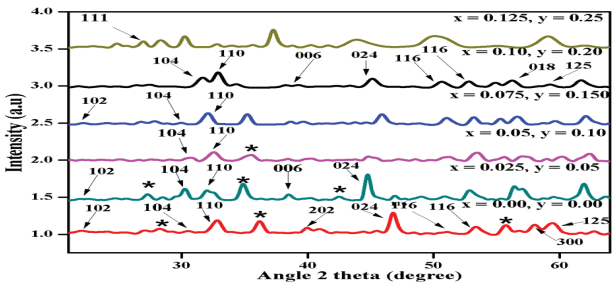

Fig. 2. XRD spectra of BYNFO, series.

Table1
Crystal lattice and physical parameters of BYNFO, series

Parameters	X = 0.00 Y = 0.00	X = 0.025 Y = 0.05	X = 0.05 Y = 0.1	X = 0.075 Y = 0.15	X = 0.1 Y = 0.2	X = 0.125 Y = 0.25
Lattice constant a (Å)	4.3893	4.3247	4.3942	4.4788	4.3071	4.4126
Lattice constant b (Å)	4.4493	4.4022	4.4030	4.178	4.4677	4.4480
Lattice constant c (Å)	14.0871	14.0616	14.052	14.0702	14.0201	14.071
Cell volume (Å)	286.07	285.706	285.11	279.84	274.89	281.14
X-ray density (g cm^{-3})	9.8	7.14	7.33	7.21	7.42	6.87
Bulk density (g cm^{-3})	6.873	6. 528	6.425	6.896	6.728	6.827
Porosity	0.494	0.432	0.387	0.331	0.349	0.372
Crystallite size (nm)	21.18	23.67	23.82	23.52	22.44	23.46

The crystalline size D_m was estimated by Debye–Scherer equation:

$$D_m = K\lambda / \beta \mathrm{Cos}\theta \quad (1)$$

In this equation, D_m is a crystallite size, K is Scherrer coefficient (0.89), β is full width at half maximum (FWHM), and λ is wavelength of X-rays. FWHM "β" is the most intense peak of the spectrum.

3.2. FTIR analysis

BYNFO-series samples were scanned from wavenumber range of 4,000–450 cm^{-1} to confirm the characteristics metal oxygen vibration bands. The characteristic stretching frequencies ~450 to 600 cm^{-1} were due to bonds of metal and oxygen, confirming the formation of BFO nanoparticles as shown in Fig. 3. Fe–O bonds showed stretching peaks at wave number 550–558 cm^{-1} in FeO_6 octahedral unit while stretching vibrations of Bi–O bond of prepared BFO appeared at ~530 cm^{-1} in FTIR spectrum. The bending vibrations of bismuth and iron with oxygen were observed at ~450 and ~440 cm^{-1}, respectively [34]. Out-of-phase vibrations of oxygen atoms in rhombohedral BFO were observed at 574 cm^{-1}. Substitution of Fe^{3+} ions with Ni^{3+} cations might be resulted in a minor increase in wave number position [35].

3.3. UV/visible analysis

To examine the optical properties, a dilute colloidal solution of BYNFO-series samples was subjected to UV/visible scan. A broad band of maximum absorption was recorded in the region of ≈390–400 nm as shown in Fig. 4. The direct energy band gap was calculated by using classical Tauc's approach. Figs. 5(a)–(f) show the transition band gap of

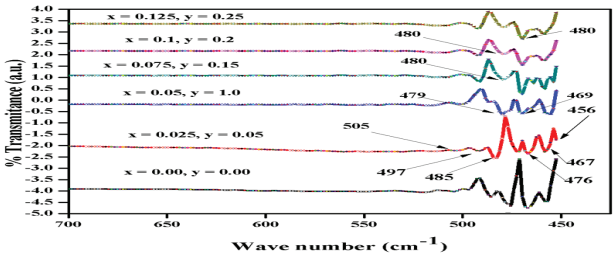

Fig. 3. FTIR spectra of BYNFO, series.

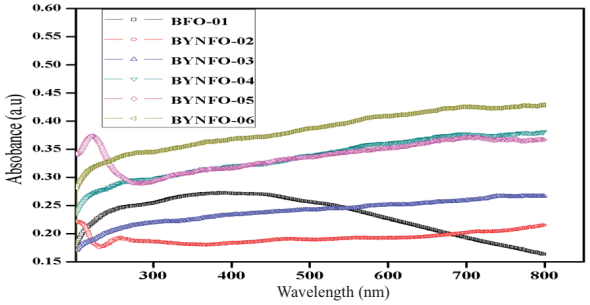

Fig. 4. UV/visible spectra of BYNFO, series.

all prepared BYFNO nanoparticles. The band-gap energy values were found to be 2.4, 1.46, 1.3, 1.33, 1.25, and 1.63 eV for BYFNO samples, respectively. The calculated value of EB gap of BFO is in the range of with previously reported values [27]. All doped BFO samples showed a drastic decrease in the optical band gap as shown in Fig. 6. This reduction in band-gap energy can be attributed to the distortion in FeO_6 octahedral structure and rearrangement of molecular orbitals due to doping of ions [16,36]. Furthermore, the role of oxygen vacancy is also a significant factor in reduction of the band gap. Yb and Ni substituted BFO ceramics exhibited energy band gap in the visible region, which makes them an appropriate substrate for photocatalytic and solar cell applications.

3.4. Current–voltage measurements

6487 Pico Ammeter/voltage source (Kiethley, USA) instrument was used at room temperature for I–V analysis of prepared BYNFO samples. I–V plot is displayed in Fig. 7. I–V output values are related to the structure and composition of the material [37]. The DC resistivity was calculated from data curves by mathematical equation given as follows:

$$\text{Resistivity } (\rho) = RA/L \quad (2)$$

The properties of substituted concentrations were examined and outcomes showed an increase in doping cations increased their insulating behavior. The electrical resistivity of all the prepared samples is provided in Table 2.

3.5. Dielectric constant (έ)

Electric polarization and measurements of current leakage were documented by LCR–Meter Waayn KERRWK (6500B), at room temperature and in the frequency range of 100 MH to 03 GHz. The effects of increase in the concentrations of doping cations on the dielectric parameters were noted as a function of applied frequency as shown in Figs. 8 and 9.

A smooth decline in dielectric constants was observed at lower frequencies with the first resonance peak at 1.88 GHz. The dielectric constant was improved by increasing concentrations of cations and peaks slightly shifted at higher frequency (200 Hz). The variation in dielectric constant, as a function of applied frequency, depends on the dispersion of constituents in the material. The change in dielectric parameters is summarized in Table 3. The presence of resonance peaks can be elucidated by applying concept of mismatching of frequency of applied AC electric pulse and resonance metal cations of the ceramic [38].

3.6. VSM analysis

Magnetic behavior of the prepared $Bi_{1-x}Yb_xNi_y\ Fe_{1-y}O_3$ nanoparticles was evaluated using VSM Lakeshore-74071. Applied magnetic field was fixed 0.000 to 10,000 Oersted. A maximum magnetic flux of 1.51 emu/g was observed at applied field of 5800 Oersted for doping concentrations y = 0.1 and x = 0.2 of ytterbium and nickel, respectively. Consequently impacts of Yb^{3+} substitutions at Bi^{3+} site and

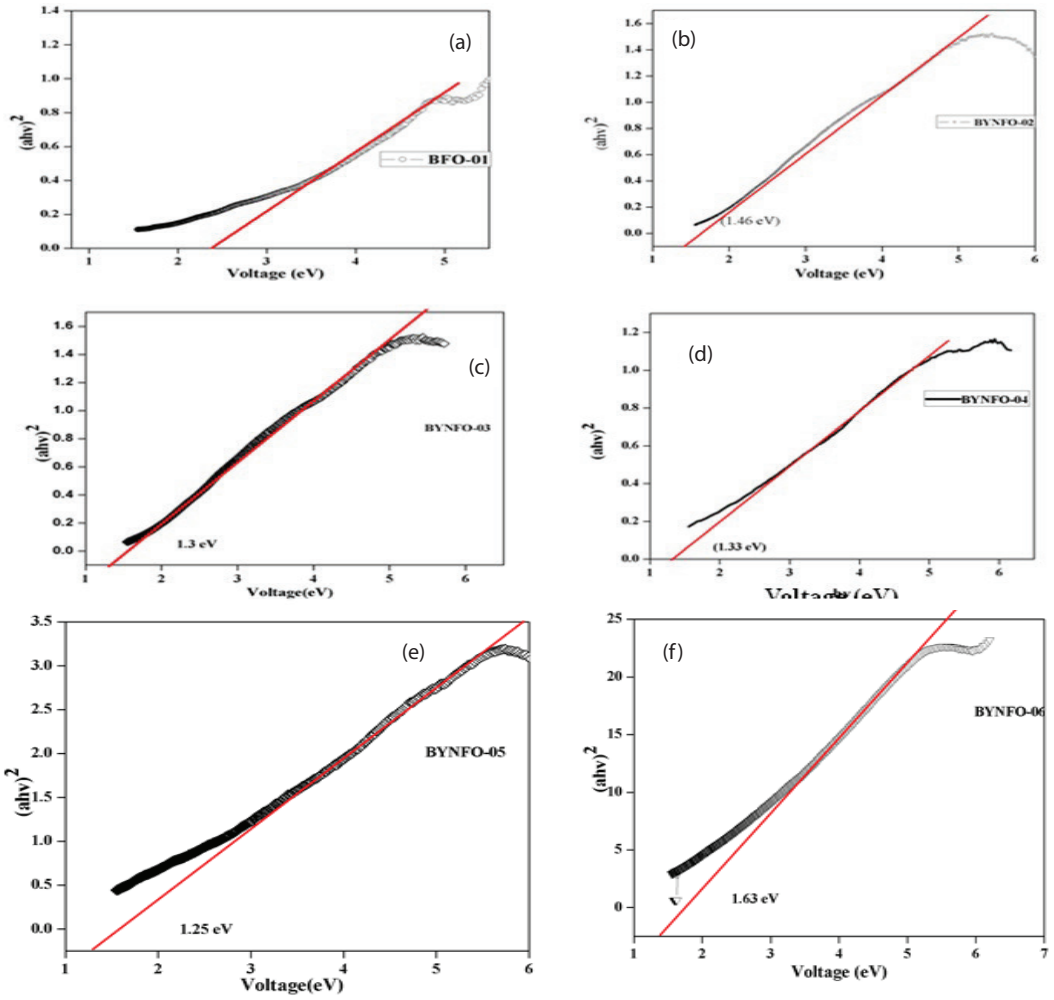

Fig. 5(a–f). Optical band gap measurement to Tauc plot for BYNFO, series.

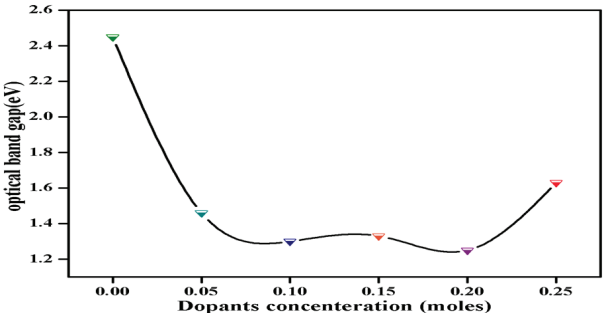

Fig. 6. Plot between optical band gap and dopants concentrations of BYNFO, series.

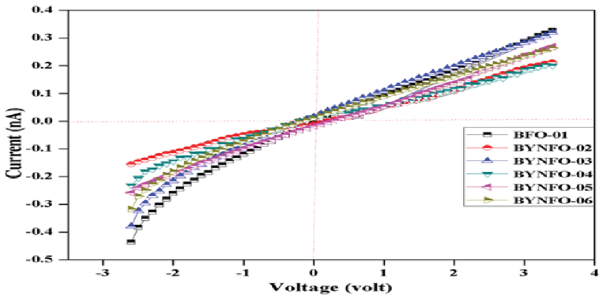

Fig. 7.Current–voltage measurements of BYNFO, series.

Ni^{3+} at Fe^{3+}enhanced magnetization >72% for BFO ceramics. The hysteresis loops of all compositions are shown in Fig. 10 and the main values of magnetic parameters are presented in Table 4.

4. Photocatalytic activity

Co-doped ceramic with composition $x = 0.10$ and $y = 0.20$ was perceived for photocatalytic degradation of by using Congo red dye ($C_{32}H_{22}N_6Na_2O_6S_2$). The trial was made for initial concentration of 0.5 ppm of CR dye in 100 mL volume containing 200 mg of photocatalytic substrate. The breakup of CR dye was charted with an interval of 3 min as shown in Fig. 11 by fixing wavelength at 510 nm(λ_{max}) for CR dye.

The photo excited semiconductor material $Bi_{1-x}Yb_xNi_yFe_{1-y}O_3$ tangled the redox reactions at the surface. Transition of valance electrons to the conduction by absorption of sunlight, eventually "hole–electron" pairs are bred at surface of photo-active substrate. Plasmon

Table 2
Resistivity measurements of BYNFO, series

Doping concentrations (moles/L)	$x = 0.000$ $y = 0.000$	$x = 0.025$ $y = 0.05$	$x = 0.05$ $y = 0.1$	$x = 0.075$ $y = 0.15$	$x = 0.1$ $y = 0.2$	$x = 0.125$ $y = 0.25$
Resistivity (Ω cm^{-1})	1.15×10^9	1.21×10^9	1.31×10^9	1.212×10^9	1.42×10^9	1.1×10^9

Table 3
Dielectric parameters for BYNFO, series

Parameters	Frequency	$X = 0.00$ $Y = 0.00$	$X = 0.025$ $Y = 0.050$	$X = 0.05$ $Y = 0.10$	$X = 0.075$ $Y = 0.15$	$X = 0.10$ $Y = 0.20$	$X = 0.125$ $Y = 0.25$
Dielectric constant	1.5 MHz	3.2055	3.4259	3.6939	3.9354	4.161	4.451
	2.0 GHz	3.1946	3.4091	3.667	3.9140	4.1502	4.4613
	2.5 GHz	3.1517	3.2861	3.4471	3.4417	3.699	4.1772

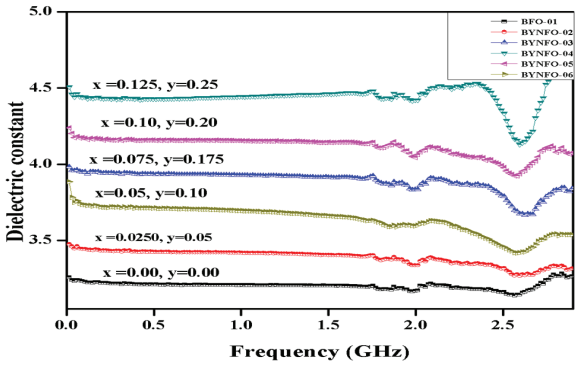

Fig. 8. Dielectric constant plot for BYNFO, series.

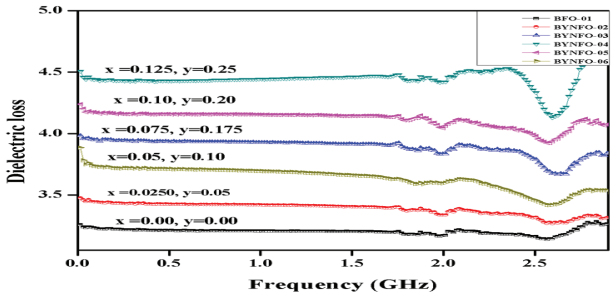

Fig. 9. Variations in dielectric loss BYNFO, series.

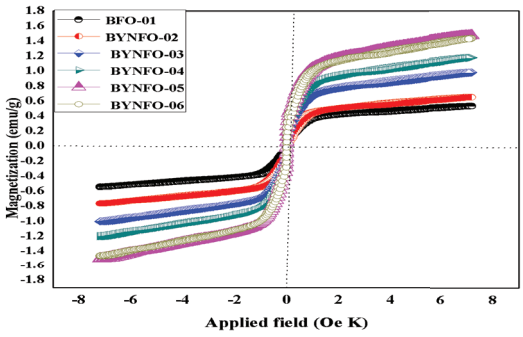

Fig. 10. M–H loop of BYNFO, series.

phenomena contribute oxidizing and reducing nature to the semiconductor. The overall expected photodegradation mechanism of Congo red dye [39] is illustrated as follows:

The hole–electron pair mechanism can be explained by photo-chemical equation as follows:

$$(Bi_{1-x}Yb_xNi_yFe_{1-y}O_3) + h\upsilon \rightarrow Bi_{1-x}Yb_xNi_yFe_{1-y}O_3 + (h + e) \quad (3)$$

The conduction band electrons harvested by solvent specie (O_2) and resulted free radical production.

$$Bi_{1-x}Yb_xNi_yFe_{1-y}O_3 + O_2 \rightarrow Bi_{1-x}Yb_xNi_yFe_{1-y}O_3\,(h) + O_2^- \quad (4)$$

The vacancy at substrate (hole) satisfied by the following chemical reaction:

$$Bi_{1-x}Yb_xNi_yFe_{1-y}O_3\,(h) + OH^- \rightarrow Bi_{1-x}Yb_xNi_yFe_{1-y}O_3 + OH^\bullet \quad (5)$$

In Eqs. (4) and (5) electron-enriched species (O_2^-) and $OH^\bullet$ were produced which are responsible for the degradation of Congo red dye.

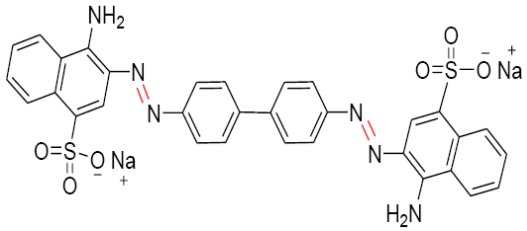

$$+ O_2^- / OH^\bullet \rightarrow \text{Degraded CR dye} + CO_2 + H_2O + SO_4^{-2} \quad (6)$$

$$\text{CR dye} + \text{Electron}_{-CB} + \text{Holes}_{+VB} \rightarrow \text{Degraded product} + \text{inorganic ions}$$

Photocatalytic productivity was derived by plotting a graph with coordinates A/A_0 as shown in Fig. 12. Around 64% of initial concentration was decomposed under visible

Table 4
Magnetic parameters of BYNFO, series

Magnetic parameters	$x = 0.000$ $y = 0.000$	$X = 0.025$ $Y = 0.05$	$X = 0.05$ $Y = 0.1$	$X = 0.075$ $Y = 0.15$	$X = 0.1$ $Y = 0.2$	$X = 0.125$ $y = 0.25$
Coercievity (Hc)/Oe	419	441	442	437	448	451
Magnetization (Ms) (emu/g)	0.22	0.65	0.99	1.6	1.51	1.42
Retentively (Mr) (emu/g)	0.09	0.41	0.64	0.73	0.89	0.86

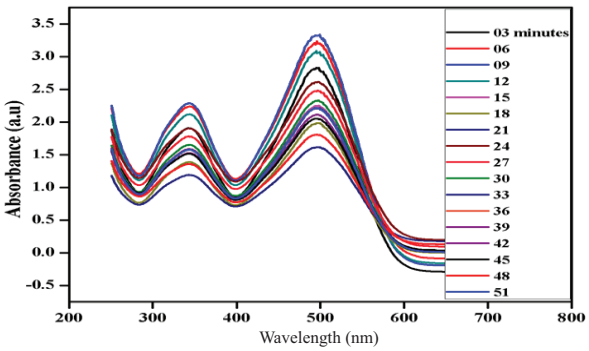

Fig. 11. Photocatalytic degradation of Congo red by BYNFO, ceramic.

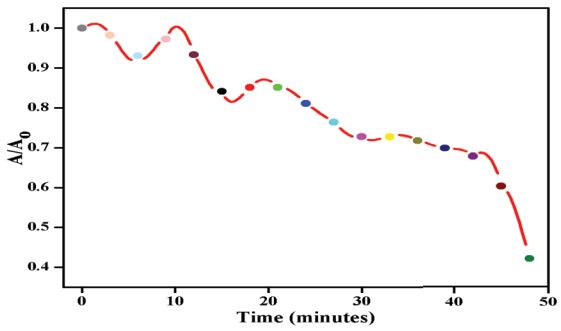

Fig. 12. A plot between A/A_0 and time (min).

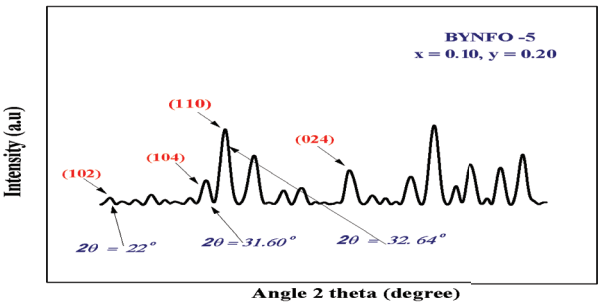

Fig. 13. Post-XRD spectra of BYNFO, series.

light. Almost 98% of ceramic was recuperated with a simple magnet bar.

4.1. Stability of co-doped BFO material

Nanoparticles of fabricated ceramic (BYNFO) were examined for chemical stability by comparing the crystal structure XRD peak patterns after application in photocatalytic degradation experiment. XRD outlines are precisely same as grew in structural elucidation before application for photocatalytic degradation as shown in Fig. 13. It could be extracted from outcomes that co-doped BNYFO nanoparticles are impervious for physical and chemical damages during the experiment.

5. Conclusion

Main focus of research was to refinement in multiferroic properties of BFO by substitution of Bi^{3+} and Fe^{3+} by Yb^{3+} and Ni^{3+} cations. The average crystallite size was observed 23.54 nm for substituted BFO particles. The XRD analysis confirmed that BFYNO ceramics crystallizes with rhombohedral R3c structure. An increasing trend in specific resistivity was observed with increase in doping cations concentrations and a highest value of 1.42×10^9 Ω cm^{-1} was recorded for x =0.125, y = 0.25.The unsubstituted BFO showed a remnant magnetization (Mr) 0.09 emu/g, however it was improved up to 0.89 emu/g for a co-doped ceramic with concentrations y = 0.1 and x = 0.2 of ytterbium and nickel, respectively. It might be due to more favorable canting dimensions for Fe^{3+} cations in the crystal and involvement of 4f–electrons of Yb^{3+} cations for ferromagnetic behavior of co-doped ceramics. Consequently Yb^{3+} replacements at Bi^{3+} vacancies and Ni^{3+} at Fe^{3+} improved the magnetic properties (~72%) of the ceramic. Photosensitive transition breach was estimated 1.25 eV through Tauc plot that was narrow as compared with than unsubstituted BFO (2.65 eV). Photocatalytic activity of substituted ceramic ($Bi_{0.90}Yb_{0.10}Ni_{0.2}Fe_{0.80}O_3$) was recorded for CR dye and 64% of initial concentration of Congo red was degraded in >50 min. These findings exposed that Ytterbium and Nickel substituted $BiFeO_3$ is a promising photocatalyst with good photocatalytic activity under visible light regime.

Acknowledgments

Authors from King Saud University (KSA) are thankful to the King Saud University for financial support via grant number RG-1438-068. Other authors are thankful to the Islamia University of Bahawalpur and Higher Education Commission of Pakistan.

References

[1] T. Hussain, S.A. Siddiqi, S. Atiq, M.S. Awan, Induced modifications in the properties of Sr doped $BiFeO_3$ multiferroics, Prog. Nat. Sci.: Mater. Int., 23 (2013) 487–492.
[2] F. Yang, F. Zhang, C. Dong, M. Tang, Magnetoelectric $Bi_{3.15}Nd_{0.85}Ti_3O_{12}$–$NiFe_2O_4$ bilayer films derived by a SOL–GEL method, Prog. Nat. Sci.: Mater. Int., 25 (2015) 361–364.

[3] M. Bibes, A. Barthélémy, Multiferroics: towards a magnetoelectric memory, Nat. Mater., 7 (2008) 425–426.
[4] D. Khomskii, Trend: classifying multiferroics: mechanisms and effects, Physics, 2 (2009) 20.
[5] H. Schmid, Multi-ferroic magnetoelectrics, Ferroelectrics, 162 (1994) 317–338.
[6] P. Suresh, P. Babu, S. Srinath, Effect of Ho substitution on structure and magnetic properties of $BiFeO_3$, J. Appl. Phys., 115 (2014) 17D905.
[7] M. Hasan, M.F. Islam, R. Mahbub, M.S. Hossain, M. Hakim, A soft chemical route to the synthesis of $BiFeO_3$ nanoparticles with enhanced magnetization, Mater. Res. Bull., 73 (2016) 179–186.
[8] K. Biswas, D. De, J. Bandyopadhyay, N. Dutta, S. Rana, P. Sen, S.K. Bandyopadhyay, P. Chakraborty, Enhanced polarization, magnetic response and pronounced antibacterial activity of bismuth ferrite nanorods, Mater. Chem. Phys., 195 (2017) 207–212.
[9] G.N. Sharma, S. Dutta, S.K. Singh, R. Chatterjee, Effect of Ni substitution on the optical properties of $BiFeO_3$ thin films, Mater. Res. Express, 3 (2016) 106202.
[10] M.K. Sharif, M.A. Khan, A. Hussain, F. Iqbal, I. Shakir, G. Murtaza, M.N. Akhtar, M. Ahmad, M.F. Warsi, Synthesis and characterization of Zr and Mg doped $BiFeO_3$ nanocrystalline multiferroics via micro emulsion route, J. Alloys Compd., 667 (2016) 329–340.
[11] W. Sakamoto, A. Iwata, M. Moriya, T. Yogo, Electrical and magnetic properties of Mn-doped 0.7 BiFeO3–0.3 PbTiO3 thin films prepared under various heating atmospheres, Mater. Chem. Phys., 116 (2009) 536–541.
[12] B. Ahmad, A. Mahmood, M.N. Ashiq, M.A. Malana, M. Najam-Ul-Haq, M.F. Ehsan, M.F. Warsi, I. Shakir, New multiferroics $BiFe_{1-2x}Al_xMn_xO_3$ nanoparticles: synthesis and evaluation of various structural, physical, electrical, dielectric and magnetic parameters, J. Alloys Compd., 590 (2014) 193–198.
[13] J. Sharma, B.H. Bhat, A. Kumar, S. Kumar, T. Kaur, B. Want, A. Srivastava, Magnetic and dielectric properties of Ce–Co substituted $BiFeO_3$ multiferroics, Mater. Res. Express, 4 (2017) 036104.
[14] L. Betancourt-Cantera, A. Bolarín-Miró, C. Cortés-Escobedo, L. Hernández-Cruz, F. Sánchez-De Jesús, Structural transitions and multiferroic properties of high Ni-doped $BiFeO_3$, J. Magn. Magn. Mater., 456 (2018) 381–389.
[15] R. Pandu, $CrFe_2O_4$–$BiFeO_3$ Perovskite multiferroic nanocomposites–a review, Mater. Sci. Res. India, 11 (2014) 128–145.
[16] B. Bhushan, A. Basumallick, S. Bandopadhyay, N. Vasanthacharya, D. Das, Effect of alkaline earth metal doping on thermal, optical, magnetic and dielectric properties of $BiFeO_3$ nanoparticles, J. Phys. D: Appl. Phys., 42 (2009) 065004.
[17] S. Pradhan, B. Roul, Effect of Gd doping on structural, electrical and magnetic properties of $BiFeO_3$ electroceramic, J. Phys. Chem. Solids, 72 (2011) 1180–1187.
[18] Z. Chen, Y. Li, Y. Wu, J. Hu, Hydrothermal synthesis and mechanism and property study of La-doped $BiFeO_3$ crystallites, J. Mater. Sci. – Mater. Electron., 23 (2012) 1402–1408.
[19] G.L. Song, H.X. Zhang, T.X. Wang, H.G. Yang, F.G. Chang, Effect of Sm, Co codoping on the dielectric and magnetoelectric properties of $BiFeO_3$ polycrystalline ceramics, J. Magn. Magn. Mater., 324 (2012) 2121–2126.
[20] S. Zhao, Q. Yun, Enhanced ferromagnetism of Ho, Mn co-doped $BiFeO_3$ nanoparticles, Integr. Ferroelectr., 141 (2013) 18–23.
[21] M. Tadic, S. Kralj, M. Jagodic, D. Hanzel, D. Makovec, Magnetic properties of novel superparamagnetic iron oxide nanoclusters and their peculiarity under annealing treatment, Appl. Surf. Sci., 322 (2014) 255–264.
[22] W. Cui, J. Li, Y. Sun, H. Wang, G. Jiang, S.C. Lee, F. Dong, Enhancing ROS generation and suppressing toxic intermediate production in photocatalytic NO oxidation on O/Ba co-functionalized amorphous carbon nitride, Appl. Catal., B, 237 (2018) 938–946.
[23] X.A. Dong, J. Li, Q. Xing, Y. Zhou, H. Huang, F. Dong, The activation of reactants and intermediates promotes the selective photocatalytic NO conversion on electron-localized Sr-intercalated g-C_3N_4, Appl. Catal., B, 232 (2018) 69–76.
[24] T. Xiong, H. Zhang, Y. Zhang, F. Dong, Ternary Ag/AgCl/BiOIO3 composites for enhanced visible-light-driven photocatalysis, Chin. J. Catal., 36 (2015) 2155–2163.
[25] Y. Li, Y. Sun, W. Ho, Y. Zhang, H. Huang, Q. Cai, F. Dong, Highly enhanced visible-light photocatalytic NO_x purification and conversion pathway on self-structurally modified g-C_3N_4 nanosheets, Sci. Bull., 63 (2018) 609–620.
[26] W. Mao, X. Wang, Y. Han, X.a. Li, Y. Li, Y. Wang, Y. Ma, X. Feng, T. Yang, J. Yang, W. Huang, Effect of Ln (Ln = La, Pr) and Co co-doped on the magnetic and ferroelectric properties of $BiFeO_3$ nanoparticles, J. Alloys Compd., 584 (2014) 520–523.
[27] T.D. Rao, T. Karthik, S. Asthana, Investigation of structural, magnetic and optical properties of rare earth substituted bismuth ferrite, J. Rare Earths, 31 (2013) 370–375.
[28] Q. Liu, A.P. Roberts, J.C. Larrasoana, S.K. Banerjee, Y. Guyodo, L. Tauxe, F. Oldfield, Environmental magnetism: principles and applications, Rev. Geophys., 50 (2012) 1–50.
[29] M. Asif, M. Nadeem, M. Imran, S. Ahmad, S. Musaddiq, W. Abbas, Z.A. Gilani, M.K. Sharif, M.F. Warsi, M.A. Khan, Structural, magnetic and dielectric properties of NiCo doped $BiFeO_3$ multiferroics synthesized via micro-emulsion route, Physica B, 552 (2019) 11–18.
[30] J. Wang, J. Neaton, H. Zheng, V. Nagarajan, S. Ogale, B. Liu, D. Viehland, V. Vaithyanathan, D. Schlom, U. Waghmare, Epitaxial $BiFeO_3$ multiferroic thin film heterostructures, Science, 299 (2003) 1719–1722.
[31] S.-M. Lam, J.-C. Sin, A.R. Mohamed, A newly emerging visible light-responsive $BiFeO_3$ perovskite for photocatalytic applications: a mini review, Mater. Res. Bull., 90 (2017) 15–30.
[32] H. Tavakkoli, D. Beiknejad, T. Tabari, Fabrication of perovskite-type oxide La0.5Ca0.5CoO3− δ nanoparticles and its dye removal performance, Desal. Wat. Treat., 52 (2014) 7377–7388.
[33] Y. Shirahata, T. Oku, Characterization and photovoltaic properties of $BiFeO_3$ thin films, Coatings, 6 (2016) 68.
[34] P. Hermet, M. Goffinet, J. Kreisel, P. Ghosez, Raman and infrared spectra of multiferroic bismuth ferrite from first principles, Phys. Rev. B, 75 (2007) 220102.
[35] H. Kumar, J.P. Singh, R. Srivastava, P. Negi, H. Agrawal, K. Asokan, FTIR and electrical study of dysprosium doped cobalt ferrite nanoparticles, J. Nanosci., 2014 (2014).
[36] S. Irfan, Y. Shen, S. Rizwan, H.C. Wang, S.B. Khan, C.W. Nan, Band-gap engineering and enhanced photocatalytic activity of Sm and Mn doped $BiFeO_3$ nanoparticles, J. Am. Ceram. Soc., 100 (2017) 31–40.
[37] N. Balke, T. Granzow, J. Rödel, Current-voltage characteristics for lead zirconate titanate bulk ceramics, J. Appl. Phys., 104 (2008) 054120.
[38] M.A. Malik, M.Y. Wani, M.A. Hashim, Microemulsion method: a novel route to synthesize organic and inorganic nanomaterials: 1st nano update, Arabian J. Chem., 5 (2012) 397–417.
[39] S. Erdemoğlu, S.K. Aksu, F. Sayılkan, B. İzgi, M. Asiltürk, H. Sayılkan, F. Frimmel, Ş. Güçer, Photocatalytic degradation of Congo Red by hydrothermally synthesized nanocrystalline TiO_2 and identification of degradation products by LC–MS, J. Hazard. Mater., 155 (2008) 469–476.